Polyoxometalate derived hierarchically structured N,P-Codoped reduced graphene oxide/MoO$_2$ composites for high performance lithium–sulfur batteries

Won Il Kim [a,1], Jeong Seok Yeon [a,1], Hyunyoung Park [b,c], Hwi Jung Kim [a], Min Ju Kim [a], Jongsoon Kim [b,c], Ho Seok Park [a,c,d,e,*]

[a] School of Chemical Engineering, Sungkyunkwan University, 2066 Seoburo, Jangan-gu, Suwon-si, Gyeonggi-do, 16419, Republic of Korea
[b] Department of Energy Science, Sungkyunkwan University, 2066 Seoburo, Jangan-gu, Suwon-si, Gyeonggi-do, 16419, Republic of Korea
[c] SKKU Institute of Energy Science and Technology (SIEST), Sungkyunkwan University, 2066 Seoburo, Jangan-gu, Suwon-si, Gyeonggi-do, 16419, Republic of Korea
[d] Department of Health Sciences and Technology, Samsung Advanced Institute for Health Sciences and Technology (SAIHST), Sungkyunkwan University, 2066 Seoburo, Jangan-gu, Suwon-si, Gyeonggi-do, 16419, Republic of Korea
[e] SKKU Advanced Institute of Nano Technology (SAINT), Sungkyunkwan University, 2066 Seoburo, Jangan-gu, Suwon-si, Gyeonggi-do, 16419, Republic of Korea

ARTICLE INFO

ABSTRACT

Lithium-sulfur batteries (LSB) have a higher energy density than a practical lithium-ion battery, but they have a number of issues, including a lithium polysulfide (LiPS) shuttle and sluggish reaction kinetics, that must be addressed before they can be used in large-scale applications. Hierarchically structured MoO$_2$ nanoparticles with N,P-codoped reduced graphene oxide (N,P-rGO/h-MoO$_2$) are prepared by the combined procedures of the Ostwald ripening process and hydrothermal treatment, followed by homogeneously distributed hollow MoO$_2$ nanospheres on N,P-codoped rGO sheets. The hollow structure of MoO$_2$ can act as a physical barrier to LiPS through its interior void and volume buffering of sulfur during cycling. In addition, N and P atoms introduced with MoO$_2$ nanoparticles not only contribute to enhanced sulfur immobilization but also promote LiPS redox kinetics. The N,P-rGO/h-MoO$_2$@S cathode materials demonstrated a high discharge capacity of 1274.9 mAh g^{-1} at 0.1C with superior high-rate capacity of 374.4 mAh g^{-1} at 10C. Furthermore, the N,P-rGO/h-MoO$_2$@S showed excellent long-term stability at 5 and 10C with low-capacity decay rates of 0.043 and 0.029% per cycle, respectively, even after 900 cycles. At a sulfur loading concentration of 4.2 mg cm^{-2}, the N,P-rGO/h-MoO$_2$@S obtained a high capacity of 5.0 mAh cm^{-2} with high-capacity retention of 79.7% over 250 cycles, and a relatively low fading rate of 0.08% per cycle.

1. Introduction

The ever-increasing development of electronic devices and electric vehicles has strong demand for advanced energy storage devices that meet the following criteria: high energy density, safety, and low cost [1–3]. Lithium-sulfur batteries (LSB) have received significant attention as an alternative to commercial lithium-ion batteries, due to their high theoretical capacity (1675 mAh g^{-1}), low cost, and resource abundance of active sulfur [4,5]. Despite these advantages, there are technical bottlenecks such as low conductivity of sulfur (5 × 10^{-30} S cm^{-1}), dissolution and occlusion of lithium polysulfide (LiPS) species, and volume expansion of sulfur (up to 80%) limiting the application of LSB

in practice [6,7].

A variety of chemical strategies have been used to address the above-mentioned limitations in the design of sulfur-hosting materials. First, carbon-based materials (CMs), including carbon nanotubes [8–10], reduced graphene oxide (rGO) [11,12], hollow carbon [13,14], carbon spheres [15,16], and carbon nanofiber [17,18] have received widespread attention due to their excellent electrical conductivity, high specific surface area, and controllable porosity [19,20]. The addition of sulfur to CMs used as host materials can improve the utilization of sulfur by providing electrical conduction pathways and a larger surface area. However, the weak interaction between CMs and LiPS continued to dissolve LiPS in the electrolyte, resulting in degradation of performance

and stability. Therefore, heteroatom doped CMs such as P, O, N, S, and P have been incorporated to create abundant polar sites for strong immobilization of LiPS [21–23]. Introducing heteroatoms into CMs improves the electronic conductivity and polarity, improving the electrochemical performance of LSBs. However, the low tab density and sulfur utilization of CMs still pose a challenge for high-power LSBs [24]. Transition metal oxides (TMOs), including CuO [25], SnO$_2$ [26], ZnCo$_2$O$_4$ [27], CoFe$_2$O$_4$ [28], MnCo$_2$O$_4$ [29], Fe$_3$O$_4$ [30], V$_2$O$_5$ [31], NiO [32], and SiO$_2$ [33] have also been studied to form polar host structures of sulfur. Although TMOs can effectively entrap LiPS through strong chemical interactions, they show low electrical conductivity, sluggish redox kinetics, and low sulfur utilization. Therefore, the hybrid of heteroatom doped CMs and TMOs is expected to act as a promising host matrix.

We present a polyoxometalate (POM)-derived hierarchically structured N,P-codoped rGO and MoO$_2$ composite in which MoO$_2$ nanorods are aggregated as secondary hollow spherical particles deposited on the large surface of N,P-codoped rGO (N,P-rGO/h-MoO$_2$), through self-assembly and Ostwald ripening process. POMs with anionic molecular metal complexes based on high-valence transition metals such as Mo, W, and V, have advantages in terms of their uniform structural diversity and size, versatile electronic properties, and multiple redox active sites [34]. In addition, the structural tunability and compositional diversity allow POMs to serve as a template and precursor for the formation of hierarchically structured TMOs [35]. In particular, phosphomolybdic acid hydrate (PAH) was selected as the POM due to its dual atom sources of Mo and P, facile conversion into MoO$_2$, and complex hollow sphere structure formation. The as-synthesized N,P-rGO/h-MoO$_2$, a hierarchically structured polar sulfur host framework, acts as an efficient redox mediator, accelerating the redox kinetics of sluggish conversion reaction. The hollow structure of MoO$_2$ acts as a physical and chemical barrier by serves both physical and chemical barrier by entrapping LiPS into the void and preventing the shuttle effect due to the donation of polar sites. In addition, the uniformly anchored hollow MoO$_2$ particles effectively prevent the restacking of the rGO sheets, resulting in a higher electrolyte penetration that induces accelerated Li$^+$/e$^-$ transport. Furthermore, the excessive LiPS dissolution was reduced by the formation of a polar surface as a result of the codoping of (N,P) heteroatoms, which provided abundant dipole polarization. Consequently, the hybridization of POM derived hierarchical MoO$_2$ with heteroatom doped rGO successively provides improved insight into the development of an efficient redox mediator for LSB.

2. Materials and methods

2.1. Synthesis of N,P-rGO/h-MoO$_2$@S

First, 600 μl of pyrrole and 25 ml of ethanol were added to the vial and sonication for 30 min (Solution A). Following immersion of 1 mmol (1825.25 mg) of PAH (H$_3$PMo$_{12}$O$_{40}$) in 100 mL of deionized (DI) water, this mixture was added in 40 ml of Graphene Oxide (GO) and then stirred for 30 min (Solution B). Then, the prepared solution A was added dropwise to solution B with vigorous stirring for 20 h. The black viscous solution was transferred to Teflon-lined stainless steel autoclave and subjected to hydrothermal treatment at 180 °C for 12 h. After a cooling to room temperature, the product was filtered by centrifugation and washed with DI water until a neutral pH. After washing, the clay-like black powder was freeze-dried for 3 days. It was then heated in Ar gas for 2 h to 500 °C. The sample was naturally cooled after heating (N,P-rGO/h-MoO$_2$). To add sulfur to the host material, the prepared N,P-rGO/h-MoO$_2$ and commercial Sulfur powder (Sigma-Aldrich) were ground using a mortar at a ratio of 1:3 followed by heating at 155 °C for 12 h in a Teflon liner under an Ar atmosphere.

2.2. Synthesis of N-rGO/MoO$_2$@S and rGO/MoO$_2$@S

Since the Phosphorus in N,P-rGO/h-MoO$_2$ is obtained from H$_3$PMo$_{12}$O$_{40}$, N-rGO/MoO$_2$ was prepared using (NH$_4$)$_6$Mo$_7$O$_{24}$•4H$_2$O instead of H$_3$PMo$_{12}$O$_{40}$. The rest of the procedure was carried out as exactly mentioned above. Since Nitrogen in N-rGO/MoO$_2$ was obtained from pyrrole, rGO/MoO$_2$ was produced without pyrrole. The rest of the process was carried out exactly as above.

2.3. Materials characterization

The high-resolution scanning electron microscopy (HR SEM, MERLIN) and transmission electron microscopy (TEM, Libra 200 HT Mc Cs, 200 kV) images were collected to determine the microstructure. The X-ray diffraction (XRD, D8, Bruker) was analyzed in a 2θ range of from 5° to 85° to obtain inherent peaks. Raman spectroscopy (SENTERRA Raman) was used with a 532 nm laser to confirm structural properties. The nitrogen adsorption-desorption isotherms, pore size distribution, specific surface area, and pore volume was measured using the Brunauer-Emmett-Teller (BET) and the Barrett-Joyner-Halenda (BJH) method using Quantachrome Nova 3200e. Thermogravimetric analysis (TGA, SDT Q600) was measured at a heating rate of 10 °C min^{-1} in N$_2$ gas. Inductively coupled plasma-optical emission spectroscopy (ICP-OES, OPTIMA 8300) was conducted to measure the molecular concentration.

2.4. Electrochemical measurements

N,P-rGO/h-MoO$_2$@S electrodes were prepared by suspending N,P-rGO/h-MoO$_2$@S powder (active materials, 80 wt%), carbon black (conductive additive; 10 wt%), and polyvinylidene difluoride (PVdF, binder, 10 wt%) in N-methyl-2-pyrrolidone (NMP). The slurry was coated onto aluminium foil using a doctor blade to give a S-loading area of 1.5 mg cm^{-2} (4.2 mg cm^{-2} for high S loading test), and dried in an oven at 80 °C for 12 h. The same procedure was also used to prepare N,P-rGO/MoO$_2$@S, N-rGO/MoO$_2$@S and rGO/MoO$_2$ electrodes for references. A Lithium foil (anode), polypropylene (PP, separator, Celgard 2400) and an electrolyte composed of 1 M bis(trifluoromethane)sulfonimide lithium (LiTFSI, Sigma-Aldrich) with 0.3 M lithium nitrate (LiNO$_3$, Sigma-Aldrich) in a v/v mixture of 1,3-dioxolane (Sigma-Aldrich) and 1,2-dimethoxyethane (Sigma-Aldrich) were used to assemble coin cells (CR2032). An electrolyte was added with E/S ratio of 10 μl per mg of sulfur. Cyclic voltammetry (CV, VMP3, Biologic) was performed at a scan rates from 0.1 to 0.8 mV s^{-1} with the potential range of 1.7–2.8 V. The electrochemical impedance spectroscopy (EIS) measurements were obtained within a frequency range of 0.01–1 × 10^6 Hz. Galvanostatic charge-discharge (GCD) profiles were measured at different C-rates (1C = 1675 mA g^{-1}).

2.5. Li$_2$S precipitation measurement

S-free electrodes fabricated as above were treated with 30 μl of 0.5 M Li$_2$S$_8$ containing electrolyte on the cathode site, and with 30 μl of 0.5 M Li$_2$S$_8$-free electrolyte on the anode site, to form a symmetric cell. The resulting cells were first discharged galvanostatically to 2.10 V at 0.05C and then discharged potentiostatically at 2.10 V for Li$_2$S nucleation and growth.

2.6. Li$_2$S$_6$ symmetric cell test

Electrodes were fabricated by mixing S-free N,P-rGO/h-MoO$_2$ (80 wt %), carbon black (10 wt%), and PVdF binder (10 wt%) in NMP. The resulting slurry was coated onto aluminium foil, and the resulting coating was dried in an oven at 80 °C for 12 h. Two of these electrodes were each treated with 30 μl 0.5 M Li$_2$S$_6$ to afford symmetric cells, which were then analyzed by CV at various scan rates (0.2, 0.5, 1.0, and 2.0

mV s^{-1}) over the potential range of −1.0 to 1.0 V.

2.7. Shuttle current measurement

The electrode was activated at 0.05 C-rate followed by discharging galvanostatically at different voltage with switching to the potentiostatic discharge for 1 h. The shuttle current was measured as potentiostatic current versus the potential drop.

2.8. Computational details

Density functional theory (DFT) calculations were performed with the Vienna Ab initio Simulation Package (VASP) [36]. Projector-augmented wave pseudopotentials were used with a plane-wave basis set, as implemented in VASP [37]. Perdew-Burke-Ernzerhof's (PBE) parametrization of the generalized gradient approximation (GGA) was used [38]. A 2 × 2 × 1 k-point grid was used for DFT calculations to calculate the MoO$_2$ surface. For more accurate calculation results for van der Waals interaction between lithium polysulfide and substrate, the DFT-D3 correction method was considered in this study [39]. A kinetic energy cutoff of used as 500 eV in all the calculations, and the overall structure was optimized until the force in the unit cell converged to within 0.03 eV Å^{-1}.
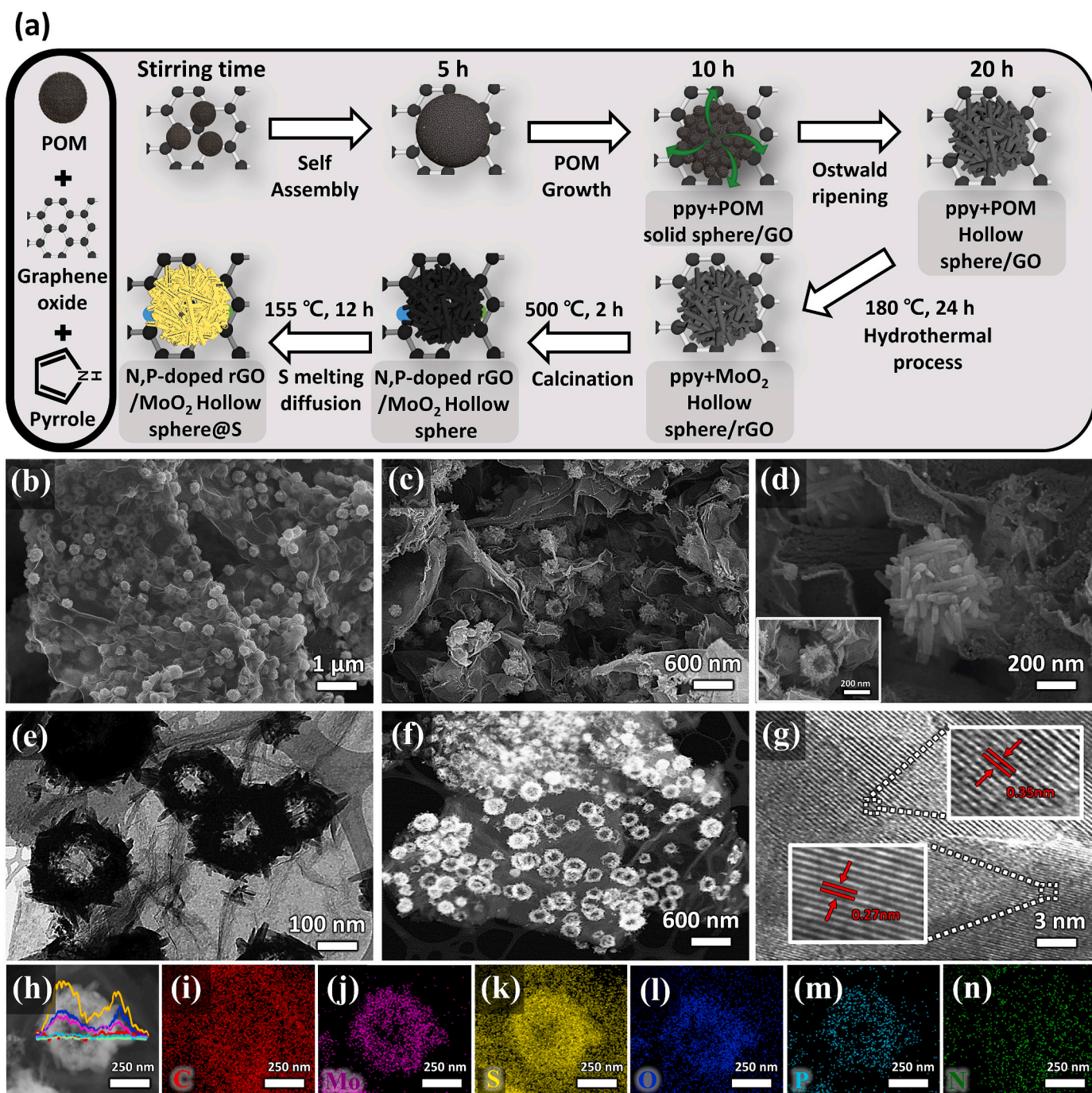

Fig. 1. (a) the schematic illustration for the synthetic procedures of N,P-rGO/h-MoO$_2$@S. SEM images of N,P-rGO/h-MoO$_2$ with (b) low-, (c) medium-, and (d) high magnification. (inset image of Fig. 1d: cracked MoO$_2$ sphere), (e) HR-TEM and (f) dark-field STEM image of N,P-rGO/h-MoO$_2$, (g) high magnification HR-TEM image of N,P-rGO/h-MoO$_2$, (h–n) line-profile and elemental mapping STEM image of N,P-rGO/h-MoO$_2$@S with (i) C, (j) Mo, (k) S, (l) O, (m) P, and (n) N.

3. Results and discussion

A schematic of the synthesis process of N,P-rGO/h-MoO$_2$@S is illustrated in Fig. 1a (see the experimental Section for further details). In the presence of pyrrole, the oxidation polymerization of pyrrole to polypyrrole (ppy) results in POM acting as a strong oxidizing agent. The driving force for self-assembly into nanoparticles (NPs) is the electrostatic interaction between negatively charged POM and positively charged ppy. A secondary hollow sphere structure was constructed by Ostwald ripening of the aforementioned self-assembled particles. POM clusters located outside the surface are gradually grown into large particles at the expense of internal POM NPs when stirring the ppy+POM/GO composite solution. During ripening, the interior cavity within the Ostwald cluster grew simultaneously, forming hollow ppy+POM NPs on the surface of GOs. Furthermore, the hydrothermal process led to the conversion of POM into MoO$_2$ and the reduction of GO to rGO. In addition, through the calcination process, N, P atomic doping were obtained from ppy and POM, respectively, to synthesize N,P-rGO/h-MoO$_2$.

The stirring time of the ppy+POM/GO solution is an essential factor for controlling the size and distribution degree of h-MoO$_2$ spheres. Fig. S1 shows that the controllable morphology of N,P-rGO/h-MoO$_2$ varies over time. Several nm-sized ppy+POM NPs were uniformly distributed on the surface of GO for 1 h, followed by self-assembled growth of solid spherical NPs over 5 h. In particular, the surface of ppy+POM NPs became rough after 10 h, indicating the formation of a rod-shaped structure on the outer of the surface. Through the Ostwald ripening process, ppy+POM NPs are gradually grown into a rod-shaped structure and form hollow spherical particles. After 20 h, the hierarchical hollow structure could not be preserved because excessive aggregation on the outer surface of ppy POM NPs caused the collapse of the spherical structure (Fig. S2). Furthermore, the quantity of precursor is another critical factor to optimize the formation of composites. The amount of pyrrole and POM could significantly affect to form hierarchically structured composites aggregated with nanorods as secondary hollow spherical particles. When a large amount of pyrrole was added, a layered structured N,P-rGO/MoO$_2$ was constructed instead of desired composites (Fig. S3a). Since the hierarchical structure is beneficial for preventing the LiPS dissolution and volume expansion, a moderate amount of pyrrole was used to form desirable structure. Moreover, an excessive amount of POM resulted in the thick POM layer with NPs deposited on the surface of rGO, impeding the smooth progress of the self-assembly process (Fig. S3b and Fig. S3c). The optimized loading content of MoO$_2$ in the N,P-rGO/h-MoO$_2$ composites were demonstrated as 28.8 wt% through the element concentration of Mo, following the typical crystalline planes of monoclinic MoO$_2$ in XRD (Table S1). The hierarchically structured N,P-rGO/h-MoO$_2$ obtained from POM was characterized using scanning electron microscopy (SEM). Compared to the SEM images of bulk aggregates of POM (Fig. S4) and rGO with a smooth surface (Fig. S5), N,P-rGO/h-MoO$_2$ (Fig. 1b and **c**) show that the h-MoO$_2$ spheres are homogenously distributed with diameters ranging from 200 to 400 nm on the N,P-codoped rGO. According to the high-magnification SEM image (Fig. 1d), the h-MoO$_2$ nanospheres had a rough outer surface covered by a random assembly to rod-shaped nanoparticles with a size of about 140 × 22 nm. Moreover, cracks with obvious cavities verify the hollow space of anchored h-MoO$_2$ nanospheres (inset in Fig. 1d). The N,P-rGO/h-MoO$_2$ was further characterized using high-resolution transmission electron microscopy (HR-TEM) and dark-field scanning transmission electron microscope (STEM). As shown in Fig. 1e and **f**, the hollow interior of h-MoO$_2$ nanospheres anchored on N,P-codoped rGO sheets was observed in the presence of nanorods. The crystalline structure of N,P-rGO/h-MoO$_2$ was identified, illustrating the (−111) and (−211) planes of MoO$_2$ with d-spacing of 0.35 and 0.27 nm, respectively (Fig. 1g). The energy dispersive X-ray (EDX) spectroscopy supports the uniform distribution of h-MoO$_2$ NPs on the rGO sheets, as shown in the Mo, C, and O signals (Figs. S6 and S7).

Moreover, N and P heteroatoms were uniformly distributed due to overlap with the C signal of rGO and Mo signal of MoO$_2$. The hierarchical structure of N,P-rGO/h-MoO$_2$ was maintained without aggregated clusters of sulfur melt-diffusion process was conducted, indicating that sulfur was homogenously dispersed in the interior cavities of N,P-rGO/h-MoO$_2$ (Fig. S8). In addition, the infiltrated sulfur was not only evenly distributed inside the h-MoO$_2$ nanospheres but also on the N,P-rGO/h-MoO$_2$ indicating polar interaction between heteroatoms and sulfur, corresponding with elemental mapping and line-profile analysis of N,P-rGO/h-MoO$_2$@S (Fig. 1h–n and Fig. S9).

The crystalline structure of the hierarchical N,P-rGO/h-MoO$_2$@S was further analyzed by X-ray diffraction (XRD) patterns (Fig. 2a). Pristine POM exhibited patterns that matched well with conventional Keggin-structured POM. The N,P-rGO/h-MoO$_2$ exhibited three dominant peaks at 25.9, 36.9, and 53.6, corresponding to (−111), (−211), and (−311), which are typical crystalline planes of monoclinic MoO$_2$ (JCPDS No. 78-1071), indicating that the POM existing in ppy+POM/GO solution was completely converted into MoO$_2$ by the hydrothermal process. This result was consistent with HR-TEM from the aforementioned Fig. 1g, indicating that the broad main diffraction peaks were affected by the nano-crystalline characteristics of h-MoO$_2$. Furthermore, these results implied that each N atom from pyrrole and each P atom from the center of POM diffused the GO surface, without forming nitrate and phosphate phases, respectively. The typical diffraction peak of rGO at 23.3 is not clearly observed due to the overlap of the weak diffraction peak with the (−111) plane of h-MoO$_2$ NPs. The N,P-rGO/h-MoO$_2$@S exhibited sublimated sulfur peaks (JCPDS No. 08-0247), which not only showed no direct chemical bonding of sulfur with h-MoO$_2$, but also exhibited fine-scale sulfur penetration into internal cavities [40].

The formation of N,P-rGO/h-MoO$_2$@S was confirmed by the Raman spectrum when compared with N,P-rGO/h-MoO$_2$, rGO, sulfur, and pristine POM (Fig. 2b). The Raman signal of POM shows a set of peaks between 100 and 300 cm^{-1} corresponding to the ν_s (Mo-O$_a$). The characteristic peaks at 622.9, 890.1, and 1003.4 cm^{-1} show the stretching vibration of ν_s (Mo–O–Mo), ν_{as} (Mo–O–Mo), and ν_s (Mo=O), respectively, indicating the typical Keggin structure of POM [41]. The peaks of POM were significantly weakened as the pristine POM was completely converted to MoO$_2$ after the thermal decomposition reaction from hydrothermal procedure. The N,P-rGO/h-MoO$_2$ exhibited distinct peaks at 815.0 and 992.0 cm^{-1}, corresponding to vibration stretching of Mo–O–Mo and Mo=O bond of MoO$_2$ [42]. The I$_D$/I$_G$ ratios of N,P-rGO/h-MoO$_2$ increased from 0.98 of rGO to 1.10, while maintaining the D and G bands of the carbon-based matrix at 1344.7 and 1591.3 cm^{-1}. This result indicated that there was a strong interaction between MoO$_2$ NPs and rGO sheets with induced defect sites induced by N, P-codoping [43]. Three common peaks of N,P-rGO/h-MoO$_2$@S, and sulfur demonstrated successful sulfur impregnation within the void of h-MoO$_2$.

The surface area and pore structure of N,P-rGO/h-MoO$_2$, and N,P-rGO/h-MoO$_2$@S were compared by investigating the N$_2$ adsorption/desorption isotherms in Fig. 2c. The hysteresis loop H3 of N,P-rGO/h-MoO$_2$ was typical, indicating the presence of mesopores formed by POM-derived h-MoO$_2$ NPs [44]. The introduction of h-MoO$_2$ NPs anchored on N,P-rGO improved the Brunauer-Emmett Teller (BET) specific surface area from 120.56 m^2 g^{-1} to 170.9 m^2 g^{-1} (Fig. S10). The improved mesopores derived from the hierarchical structure not only allowed sufficient penetration of the electrolyte beneficial for Li$^+$ ion transportation but also mitigated the volumetric expansion of sulfur during lithiation/delithiation. The specific surface area of N,P-rGO/h-MoO$_2$@S was drastically reduced to 1.5 m^2 g^{-1} compared to the loosely reduced value of rGO (24.09 m^2 g^{-1}). This result demonstrated the successful infiltration of sulfur into the framework due to the combined synergetic effect of the polar nature of h-MoO$_2$ and the dipole polarization caused by codoping with heteroatoms.

To verify the dual LiPS anchoring capability of N,P-rGO/h-MoO$_2$, the displayed LiPS adsorption experiments were performed in a 5 mM
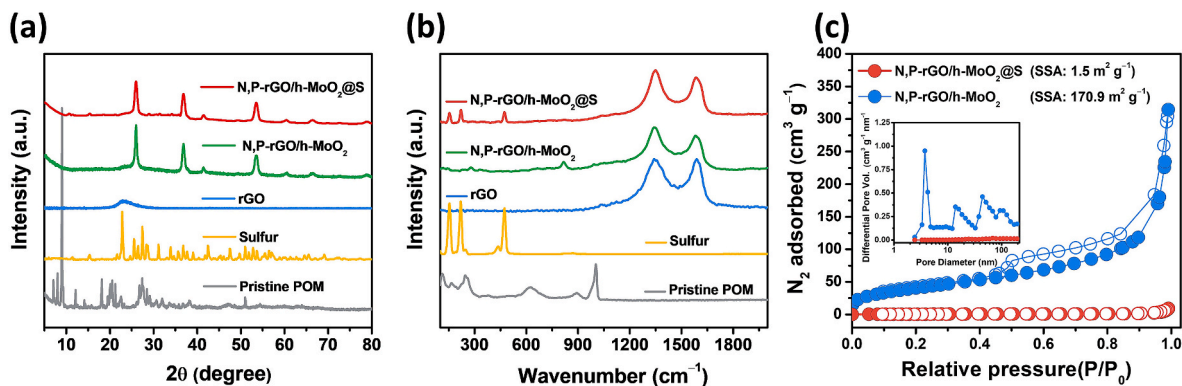
Fig. 2. (a) XRD spectra and (b) Raman spectra of N,P-rGO/h-MoO$_2$@S in comparison with N,P-rGO/h-MoO$_2$, rGO, sulfur, pristine POM, (c) N$_2$ adsorption/desorption isotherms of N,P-rGO/h-MoO$_2$@S and N,P-rGO/h-MoO$_2$. (inset pore distribution).

solution of Li$_2$S$_6$ with 0.5 M LiTFSI in a 1:1 v/v mixture of 1,3-dioxolane and 1,2-dimethoxyethane (inset in Fig. 3a). The chemically prepared LiPS solution with N,P-rGO/h-MoO$_2$ became colorless while the solution with rGO remained approximately same, validating the strong adsorption capacity of N,P-rGO/h-MoO$_2$ with polar framework. The UV–vis spectra in Fig. 3a further verify the exceptional LiPS adsorption capacity of N,P-rGO/h-MoO$_2$. A typical strong absorption peak from 250 to 350 nm indicating S$_6^{2-}$ species apparently disappeared after adding N,P-rGO/h-MoO$_2$, validating the reduced LiPS concentration. Therefore, the soluble LiPS produced during the charge/discharge processes is rapidly adsorbed by N,P-rGO/h-MoO$_2$, mitigating the excessive migration of LiPS into the electrolyte.

The electronic states and surface composition of N,P-rGO/h-MoO$_2$ were further investigated using X-ray photoelectron spectroscopy (XPS). In Fig. S11, the survey spectrum of N,P-rGO/h-MoO$_2$ showed that it had C, O, N, P, and Mo components that derived from rGO, ppy, and POM.

The XPS spectra of Mo 3d (Fig. 3b) exhibited distinct peaks located at 235.5 and 232.3 eV, corresponding to Mo^{6+} 3d$_{3/2}$ and Mo^{6+} 3d$_{5/2}$, and the peaks at 231.7 and 228.5 eV belong to the 3d$_{3/2}$ and 3d$_{5/2}$ of Mo^{4+} respectively. After adsorbing Li$_2$S$_6$, peaks located at 233.4, and 230.2 eV assigned to Mo^{5+} were newly formed, indicating the formation of a strong chemical bond in the process of electron transfer. Furthermore, all Mo 3d peaks shifted towards lower binding energy with the enhanced intensity of Mo^{4+}, forming thiosulfate and polythionate complex species. In terms of S 2p (Fig. 3c), the XPS spectra of N,P-rGO/h-MoO$_2$ after adsorption LiPS exhibited the distinct peaks located at 168.8 and 168.3 eV in the region of high binding energy, which corresponds to polythionate complexes and thiosulfate such as SO$_4^{2-}$, S$_2$O$_3^{2-}$ [45,46], and 164.1 and 163.5 eV representing the bridging sulfur (S$_B$) and terminal sulfur (S$_T$) in the region of low binding energy. Compared to the rGO after adsorption LiPS, the distinct peaks of N,P-rGO/h-MoO$_2$ shifted to higher values, which is associated with the strong chemical interaction
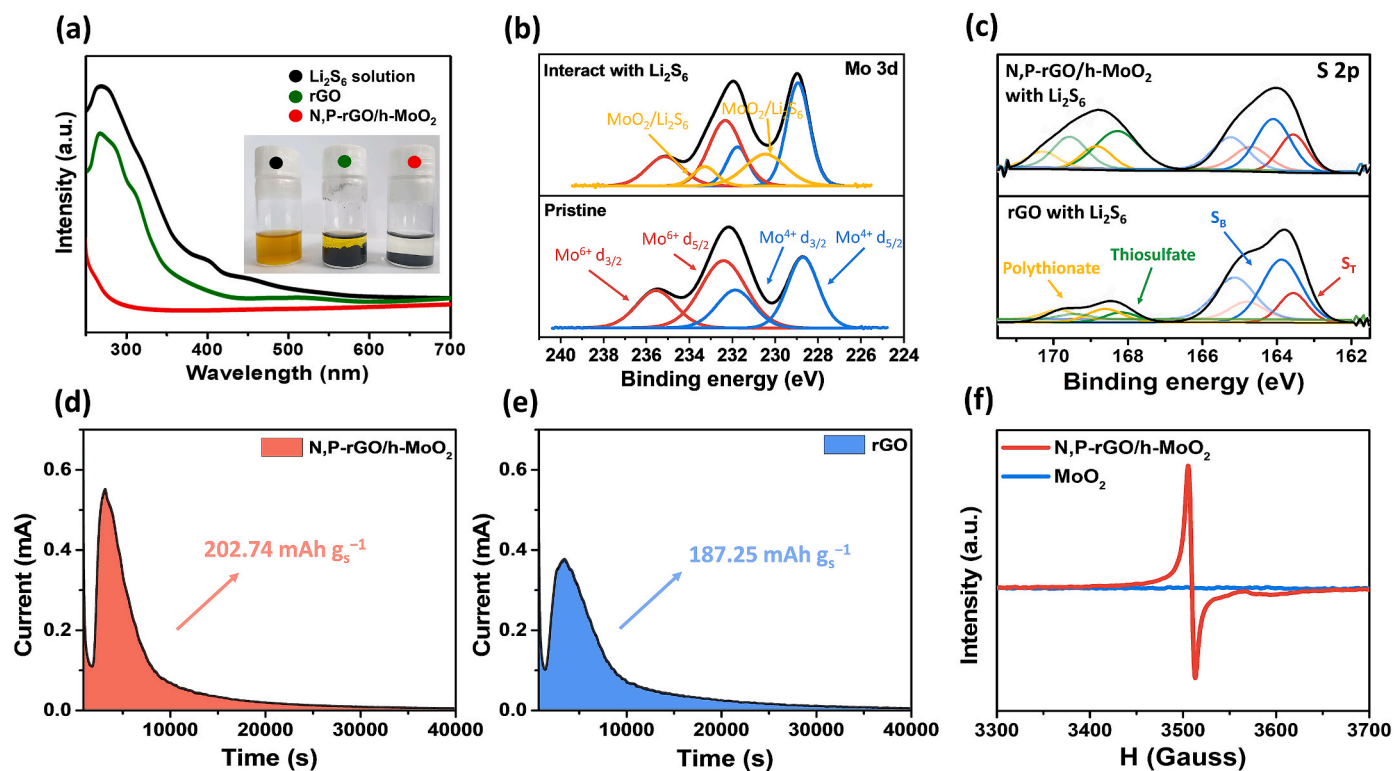

Fig. 3. (a) UV–vis spectra of N,P-rGO/h-MoO$_2$ compared with rGO after adsorption with Li$_2$S$_6$ (inset image: optical images of the above solutions). High-resolution XPS profiles of (b) Mo 3d of N,P-rGO/h-MoO$_2$ before and after adsorption of LiPS, (c) S 2p peaks of N,P-rGO/h-MoO$_2$ and rGO after adsorption of LiPS. (d), (e) Potentiostatic nucleation profiles of Li$_2$S$_8$ solution on N,P-rGO/h-MoO$_2$ and rGO electrodes. (f) EPR signal of N,P-rGO/h-MoO$_2$ and pristine MoO$_2$.

between the LiPS and N,P-rGO/h-MoO$_2$. Moreover, N,P-rGO/h-MoO$_2$ promoted the formation of polythionate and thiosulfate complex, acting as surface-bound active redox mediator to create intermediate complexes [47].

In the XPS spectra of O 1s (Fig. S12a), the peak at 533.3 eV indicates residual oxygen groups on the surface. The peaks at 531.7 and 530.2 eV are associated with the lattice O from MoO$_2$. After adsorbing LiPS, the residual O acted as active sites for the formation of sulfate species. Furthermore, the O 1s peaks shifted to lower binding energies, indicating enhanced electron cloud density on the surface due to the formation of sulfur complex species. The N 1s region shown in Fig. S12b was deconvoluted into four peaks at 401.3, 399.7, 397.9, and 396.2 eV, which are assigned to Graphitic N, Pyrrolic N, Pyridinic N, and N–Mo, respectively [48]. Each N atom can adsorb LiPS in different ways through diverse mechanisms [49]. In particular, the locations of the peaks of Graphitic N and Pyridinic N were significantly shifted towards

higher binding energies after adsorbing Li$_2$S$_6$, indicating that the negatively charged N was successfully combined with the positively charged Li of LiPS. In the XPS spectra of P 2p, two peaks at 133.8 (P–C) and 133.1 eV (P–O) were observed, as shown in Fig. S12c. Whether or not Li$_2$S$_6$ adsorption occurred did not influence the P 2p peak location, indicating that the doped P atoms did not directly contribute to the mitigation of excessive LiPS dissolution. However, it is noteworthy that the presence of P atoms with a larger atomic size and higher electron-donating capability than N led to a synergic effect with N atoms, as they ensured efficient electron transfer and provided abundant redox mediating sites [50]. Consequently, the presence of N and P atoms in N,P-rGO/h-MoO$_2$ improved the LiPS conversion kinetics.

Fig. 3d and **e** showed the potentiostatic discharge profiles of sulfur-free electrodes in a 0.5 M Li$_2$S$_8$ electrolyte to understand the redox-mediated effect of N,P-rGO/h-MoO$_2$ on Li$_2$S precipitation (see the experimental section for more details). Based on Faraday's law, the Li$_2$S
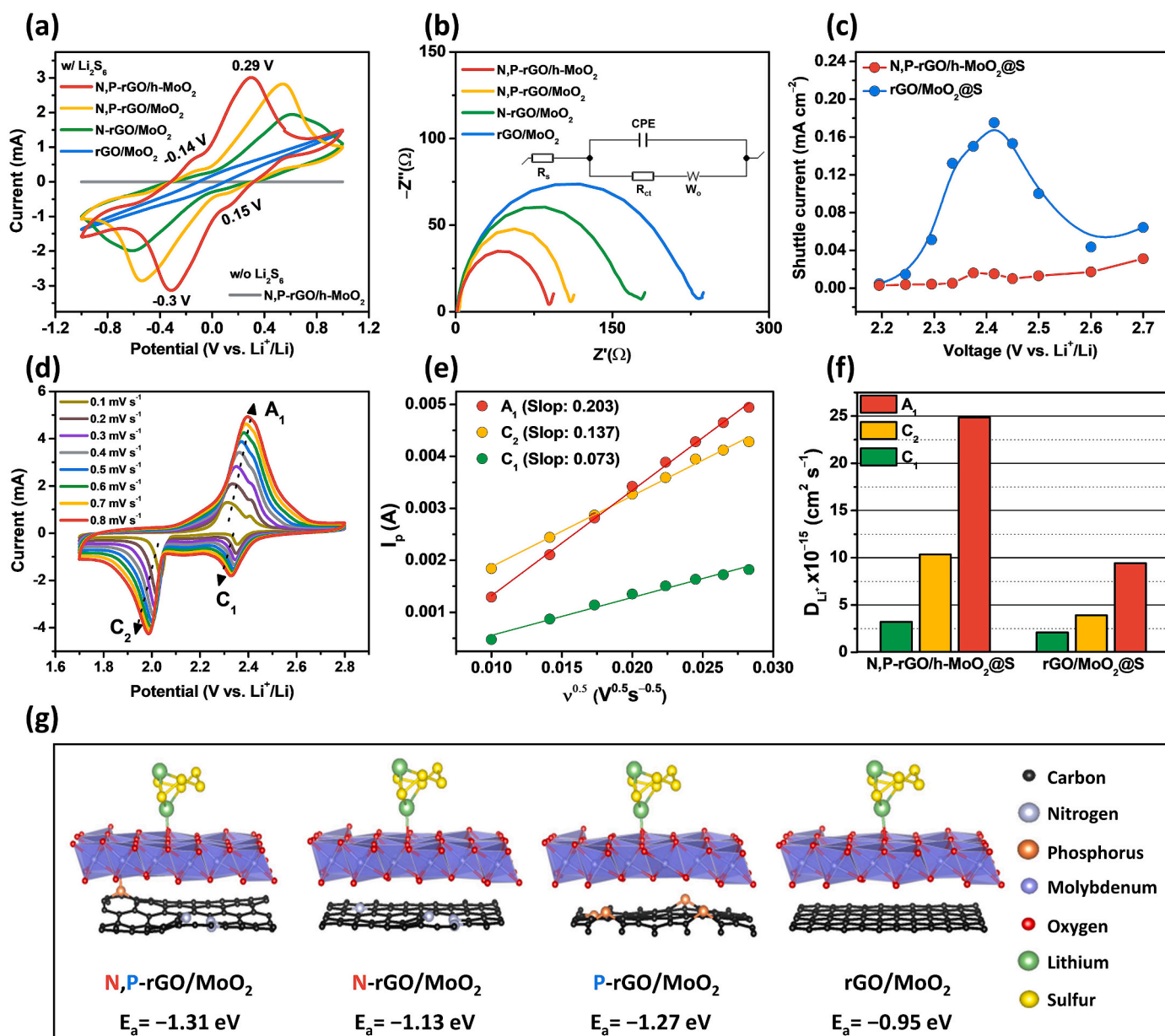

Fig. 4. (a) CV curves of symmetric cells, (b) Nyquist plots of symmetric cells with N,P-rGO/h-MoO$_2$ compared with N,P-rGO/MoO$_2$, N-rGO/MoO$_2$, and rGO/MoO$_2$. (c) the shuttle current values of the LSB cell with N,P-rGO/h-MoO$_2$@S and rGO/MoO$_2$@S cathode. (d) CV curves of N,P-rGO/h-MoO$_2$@S cathode obtained in the range of 0.1–0.8 mV s^{-1}. (e) plots of current values versus square root N,P-rGO/h-MoO$_2$@S at A$_1$, C$_1$, and C$_2$ peaks in CV curves, (f) Li ion diffusion coefficients of N, P-rGO/h-MoO$_2$@S and rGO/MoO$_2$@S. (g) DFT calculation of N,P-rGO/MoO$_2$ with heteroatom variation.

precipitation capacity was calculated to be 202.74 mA h g_s^{-1} and 187.25 mA h g_s^{-1} for the N,P-rGO/h-MoO$_2$ electrode and the rGO electrode, respectively. Also, the accelerated kinetics of the N,P-rGO/h-MoO$_2$ electrode were observed further from the earlier reduction peak (3029 s) compared to rGO (3660 s). These results suggest that the polar nature of N,P-rGO/h-MoO$_2$ provides more active sites for Li$_2$S precipitation, which facilitates the formation of Li$_2$S nuclei, which affects the entire reduction kinetics of LiPS transformation. Electron paramagnetic resonance (EPR) spectroscopy was further analyzed to understand the defect and electron configuration of N,P-rGO/MoO$_2$, which can provide favorable LiPS adsorption capacity on active sites (Fig. 3f). The POM derived N,P-rGO/h-MoO$_2$ demonstrated a unique EPR signal, which verifies the presence of unpaired electrons in oxygen vacancies compared to pristine MoO$_2$. The crystal structure of the POM derived N, P-rGO/h-MoO$_2$ was reordered by oxygen vacancies, which acted as a superficial donor, inducing fast charge transfer kinetics and supporting structure maintenance during the charge/discharge process. Furthermore, oxygen vacancies can act as effective active sites for Li$_2$S precipitation [51,52]. Given by the observed increase in the EPR signal with an increasing amount of POM, it can be inferred that a large quantity of POM precursor is attributed to an increase in oxygen vacancies (Fig. S13). Nonetheless, the amount of POM was optimized to construct hierarchically structured N,P-rGO/h-MoO$_2$, which serves as a physical and chemical barrier for LiPS (Figs. S3b and S3c).

To verify the obtained hierarchically structured N,P-rGO/h-MoO$_2$@S with the excellent electrochemical performance of POM, samples without internal void and polar substrate were prepared (see an experimental section for more details). Interestingly, N-rGO/MoO$_2$@S composite using a widely used Mo source (ammonium molybdate: (NH$_4$)$_6$Mo$_7$O$_{24}$•4H$_2$O) instead of POM showed spherical NPs without hollow interior voids (Fig. S14). Polarization cyclic voltammetry (CV) experiments were conducted to evaluate the electrocatalytic effect of N, P-rGO/h-MoO$_2$ on LiPS redox reactions in 0.5 M Li$_2$S$_6$ electrolyte (Fig. 4a). Regardless of the hierarchical structure with heteroatom codoping, the presence of MoO$_2$ revealed two reversible redox peaks. However, N,P-rGO/h-MoO$_2$ showed the smallest voltage hysteresis and the highest current density, indicating its superior conversion of LiPS. The peaks of N,P-rGO/h-MoO$_2$ at −0.14/0.15 V correspond to the conversion of S$_8$ into long-chain LiPS, while the peaks at −0.3/0.29 V attributed to Li$_2$S$_2$/Li$_2$S precipitation from long-chain LiPS. N,P-rGO/h-MoO$_2$ not only effectively adsorbed LiPS but also accelerated the redox kinetics of LiPS due to the efficiency of linking the anchored h-MoO$_2$ and N,P-doped atoms. Additionally, Fig. 4b shows symmetrically constructed cells' electrochemical impedance spectroscopy (EIS) spectra. These plots showed that the N,P-rGO/h-MoO$_2$ electrode had a lower charge transfer resistance (R$_{ct}$; 89 Ω) than those of N,P-rGO/MoO$_2$ (R$_{ct}$; 110 Ω), N-rGO/MoO$_2$ (R$_{ct}$; 177 Ω), and rGO/MoO$_2$ (R$_{ct}$; 235 Ω). The significantly reduced R$_{ct}$ value indicates the enhancement of LiPS redox kinetics by N,P-rGO/h-MoO$_2$, which can act as a redox mediator. The value of LiPS inhibiting the ability of N,P-rGO/h-MoO$_2$@S was estimated by the current shuttle measurement obtained through the natural process (Fig. 4c) [53]. The thermogravimetric analysis (TGA) indicated that the sulfur content of the N,P-rGO/h-MoO$_2$@S was estimated as 74.1 wt% (Fig. S15). The current shuttle values of the rGO/MoO$_2$@S electrode drastically increased to 2.4 V, corresponding to the solid-to-liquid phase transition of cyclic S$_8$ to soluble long-chain LiPS. In contrast, the current shuttle profile of the N,P-rGO/h-MoO$_2$@S electrode showed dramatically decreased current over the entire LiPS conversion voltage, indicating the soluble LiPS could be effectively entrapped inside the h-MoO$_2$, acting as a volume buffer layer.

In order to verify the enhanced electrochemical properties of the N,P-rGO/h-MoO$_2$@S electrode (Fig. 4d), the CV was measured under various scan rates of 0.1–0.8 mV s^{-1}. Compared to rGO/MoO$_2$@S (Fig. S16a), N, P-rGO/h-MoO$_2$@S showed significantly reduced polarization due to accelerated electron/ion transport. The Li$^+$ diffusion coefficient value

was estimated based on the following Randles–Ševčík equation:

$$I_P = 2.69 \times 10^5 n^{1.5} A D_{Li}^{0.5} C v^{0.5} C_{Li}$$

where I_p is the peak current, n is the electron charge transfer number (n is 2 for the LSB), A is the electrode area, D_{Li} is the diffusion coefficient of Li$^+$, ν is the potential scan rate, C$_{Li}$ is the Li$^+$ concentration of the electrolyte. The linear relationship between peak current and the square root of the scan rate of N,P-rGO/h-MoO$_2$@S compared to rGO/MoO$_2$@S was obtained, as shown in Fig. 4e and Fig. S16b. From the Randles–Ševčík equation, the Li$^+$ diffusion coefficient of N,P-rGO/h-MoO$_2$@S was calculated as $D_{Li}^{C1} = 1.02 \times 10^{-7}$ cm s^{-1} $D_{Li}^{C2} = 1.58 \times 10^{-7}$ cm s^{-1}, and $D_{Li}^{A1} = 5.67 \times 10^{-8}$ cm s^{-1} respectively (rGO/MoO$_2$@S: $D_{Li}^{C1} = 6.26 \times 10^{-8}$ cm s^{-1}, $D_{Li}^{C2} = 9.71 \times 10^{-8}$ cm s^{-1}, and $D_{Li}^{A1} = 4.56 \times 10^{-8}$ cm s^{-1}). The diffusion coefficient increased dramatically at the rate-determining steps of the charge/discharge processes (charge: oxidation of solid Li$_2$S$_2$/Li$_2$S to liquid Li$_2$S$_4$, discharge: reduction of liquid Li$_2$S$_4$ to solid Li$_2$S$_2$/Li$_2$S) with the most significant positive Gibbs free energy [54].

The electrocatalytic performances mentioned above demonstrated the exceptional redox mediating ability of MoO$_2$ incorporated on N,P-doped rGO. Density functional theory (DFT) was further performed to determine the interactive chemistry of composites. As shown in Fig. 4g, models with heteroatom variation were used in DFT calculation to represent MoO$_2$ on the codoped rGO surface. The theoretical adsorption energy (E$_{ads}$) was calculated using the following equation:

$$E_{ads} = E_{surface/Li_2S_6} - \left(E_{surface} + E_{Li_2S_6} \right)$$

where E$_{surface/Li_2S_6}$ is equal to the total energy of surface adsorbing Li$_2$S$_6$; and E$_{surface}$ and E$_{Li_2S_6}$ are the total energy of surface and Li$_2$S$_6$, respectively. The E$_{ads}$ of LiPS on the MoO$_2$ of N,P-rGO/MoO$_2$ was calculated to be −1.31 eV, superior to that of N-rGO/MoO$_2$ (−1.13 eV), P-rGO/MoO$_2$ (−1.27 eV), rGO/MoO$_2$ (−0.95 eV) and MoO$_2$ (−1.20 eV) (Fig. S17). These computational results suggested that the polar substrate with heteroatom codoping could enhance LiPS capture efficiency compared to the non-doped rGO surface. Due to the lower ionization energy and higher electron-donating ability of phosphorus compared to nitrogen, the E$_{ads}$ of the phosphorus-doped surface is higher than that of the nitrogen doped surface [55]. Moreover, the overall Li$_2$S$_n$ adsorption capacity of N,P-rGO/MoO$_2$ is illustrated in Fig. S18, indicating the excellent LiPS conversion kinetics of the whole reaction of N,P-rGO/-MoO$_2$. DFT calculation cannot indicate that the hollow sphere structure of N,P-rGO/h-MoO$_2$ with quantitative oxygen vacancies (h-MoO$_2$) has the enhanced adsorptive-electrocatalytic performance. Thus, POM derived N,P-rGO/h-MoO$_2$ is expected to show superior performance in practical LSB.

Fig. 5a showed the CV profiles of N,P-rGO/h-MoO$_2$@S with N,P-rGO/MoO$_2$@S, N-rGO/MoO$_2$@S and rGO/MoO$_2$@S cathode between 1.7 and 2.8 V at a scan rate of 0.1 mV s^{-1}. Two distinct cathodic peaks are observed at 2.35 and 2.04 V, which corresponds to a solid to liquid transition at higher potential (from S$_8$ to Li$_2$S$_4$) and a further reduction process, which corresponds to a solid transition from Li$_2$S$_4$ to Li$_2$S$_2$/Li$_2$S at lower energies. Conversely, two distinct anodic peaks at 2.32 and 2.41 V are attributed to converting insoluble high-chains LiPS and S$_8$. The CV curve of rGO/MoO$_2$@S showed significantly weaker current intensity and broad peaks, indicating relatively sluggish redox kinetics. For the N,P-rGO/MoO$_2$@S cathode, there is a difference in the current response in the CV profiles despite the similar composition to the N,P-rGO/h-MoO$_2$@S. This suggested that the hollow spherical structure of N,P-rGO/h-MoO$_2$@S contributed to the improvement of sulfur utilization while providing any additional capacity as a suitable host materials (Fig. S19). Therefore, the CV curve of N,P-rGO/h-MoO$_2$@S showed a distinct shift in both redox peaks intensity, suggesting the notably reduced polarization and accelerating the LiPS redox conversion reactions due to the synergic effect of hollow structure of MoO$_2$ NPs and N,
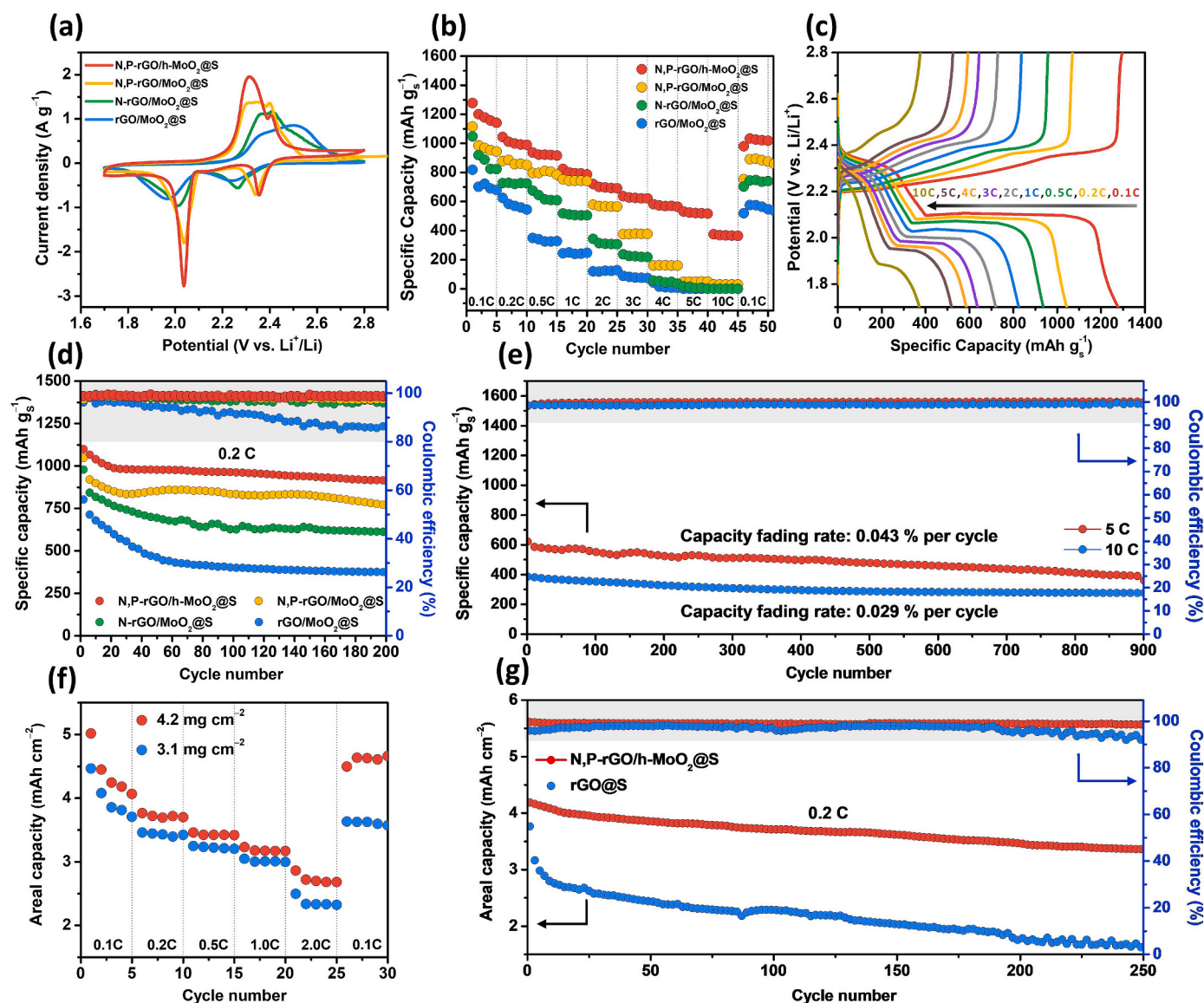
Fig. 5. (a) CV profiles (0.1 mV s^{-1}), (b) rate performance from 0.1 to 10.0C of LSB cells with N,P-rGO/h-MoO$_2$@S in comparison with N,P-rGO/MoO$_2$@S, N-rGO/MoO$_2$@S, and rGO/MoO$_2$@S. (c) GCD profiles corresponding to different C-rate of N,P-rGO/h-MoO$_2$@S, (d) cycling performance of N,P-rGO/h-MoO$_2$@S at 0.2C in comparison with N,P-rGO/MoO$_2$@S, N-rGO/MoO$_2$@S, and rGO/MoO$_2$@S, (e) long-term cycling stability of N,P-rGO/h-MoO$_2$@S at 5.0 and 10.0C. (f) rate performance of areal discharge capacity at 0.1, 0.2, 0.5, 1.0, and 2.0C with different high mass-loading electrodes, (g) the cycling stability at 0.2C with sulfur loading of 4.2 mg cm^{-2}.

P-doped atoms.

The rate capability of N,P-rGO/h-MoO$_2$@S incorporating the hierarchical structure and heteroatom doping substantially enhanced the LiPS conversion kinetics (Fig. 5b). The N,P-rGO/h-MoO$_2$@S electrode achieved reversible specific capacity of 1274.0 mAh g^{-1}, 1043.5 mAh g^{-1}, 936.4 mAh g^{-1}, 824.6 mAh g^{-1}, 530.5 mAh g^{-1}, and 374.4 mAh g^{-1} at 0.1, 0.2, 0.5, 1.0, 5.0, and 10.0C, respectively. In addition, the high discharge capacity of 1040.5 mAh g^{-1} demonstrated the excellent reversibility and rapid reaction kinetics of N,P-rGO/h-MoO$_2$@S despite the sudden reduction of the current rate to 0.1C. Furthermore, after 3.0C of N,P-rGO/h-MoO$_2$@S as a spherical hollow structure, there was a significant difference in electrochemical performance between N,P-rGO/h-MoO$_2$@S and N,P-rGO/MoO$_2$@S satisfied electrolyte penetration into the internal structure of N,P-rGO@h-MoO$_2$@S, providing improved kinetics and improved sulfur utilization of active materials. As a result, dual atom doping on rGO enhanced the overall rate performances, while the deficient LiPS adsorption of N,P-rGO/MoO$_2$@S was complemented by the hollow spherical structure of MoO$_2$ NPs. These

results are consistent with DFT calculation results showing the effect of heteroatoms. Fig. 5c showed that the charge and discharge profiles derived from galvanostatic charge/discharge curves at various current densities in N,P-rGO/h-MoO$_2$@S had significantly less polarization. Even at very high rates at 10C, two distinct plateaus were still observed in discharge profiles, which were attributed to enhanced electron transport by N, P atoms and spherical hollow structure of MoO$_2$ NPs.

The cycling performance of N,P-rGO/h-MoO$_2$@S was investigated at 0.2C compared to N,P-rGO/MoO$_2$@S, N-rGO/MoO$_2$@S, and rGO/MoO$_2$@S (Fig. 5d). Due to its polar nature and lack of structure effect, rGO/MoO$_2$@S had a low initial specific capacity (801. 9 mAh g^{-1}) and low coulombic efficiency (C.E.). In comparison, N,P-rGO/h-MoO$_2$@S exhibited a high initial discharge capacity (1098.5 mAh g^{-1}), a high capacity-retention of 82.2% and a low capacity fading rate of 0.082% per cycle, which were superior to those of the N,P-rGO/MoO$_2$@S (capacity retention = 73.8%; capacity fading rate = 0.13%), N-rGO/MoO$_2$@S (capacity retention = 61.3%; capacity fading rate = 0.19%), and rGO/MoO$_2$@S (capacity retention = 46.0%; capacity fading rate =

0.216%). The long-term stability of N,P-rGO/h-MoO$_2$@S at high rates of 5.0 and 10.0C was also investigated in Fig. 5e, under these conditions, it has a high C.E. up to 900 cycles with very ultra-low-capacity degradation. The rates are 0.043% (5.0C), and 0.029% (10.0C) respectively. The strong chemical interactions of N,P-rGO/h-MoO$_2$ reduce the shuttle effect caused by excess LiPS while also acting as a physical barrier to reduce sulfur expansion during the lithiation/delithiation processes. It is noteworthy that the electrochemical performance of N,P-rGO/MoO$_2$@S for LSB outperformed that of the previous materials (Table S2).

To verify the feasibility of N,P-rGO/h-MoO$_2$@S as a practical application requiring high energy density, LSB electrodes with high sulfur loading compared to rGO@S were fabricated. As shown in Fig. 5f, the rate and cycling performances of N,P-rGO/h-MoO$_2$@S were investigated with sulfur loadings of 3.1 and 4.2 mg cm^{-2}, with low electrolyte usage (E/S ratio = 10). The N,P-rGO/h-MoO$_2$@S with a sulfur loading of 4.2 mg cm^{-2} achieved reversible partial capacities of 5.0, 3.8, 3.4, 3.2, and 2.9 mAh cm^{-2}, at 0.1, 0.2, 0.5, 1.0 and 2.0C respectively. The electrode 4.2 mg cm^{-2} sulfur loading demonstrated 690 mAh g^{-1} at 2.0C, indicating improved electrolyte penetration by the self-assembled rod-shaped nanoparticles and confirming the stable redox kinetics even at high sulfur concentrations. Moreover, N,P-rGO/h-MoO$_2$@S maintained a high areal capacity of 3.3 mAh cm^{-2} over 250 cycles with a with high-capacity retention of 79.7% and a relatively low-capacity fading rate of 0.08% per cycle, while the rGO@S electrode suffered from severe capacity decay (0.22%) due to continuous dissolution of LiPS inducing shuttle effect (Fig. 5g).

4. Conclusions

In this work, we designed a POM derived hierarchically structured N,P-rGO/h-MoO$_2$ composite, where MoO$_2$ nanorods are incorporated as secondary hollow spherical particles deposited on a large surface of N,P-codoped rGO. The electrochemical results confirmed that the MoO$_2$ hollow spherical structure acts as a physical buffer layer entrapping the LiPS inside the void and as well as a chemical barrier preventing the shuttle effect by providing a polar surface. Moreover, the heteroatom codoped rGO provided abundant polar nature for the redox accelerator. As a result, N,P-rGO/h-MoO$_2$ acted as an effective redox mediator, exhibiting a high initial specific capacity of 1274.9 mAh g^{-1} at 0.1C and a high rate capability of 374.4 mAh g^{-1} at 10.0C. Furthermore, the N,P-rGO/h-MoO$_2$@S showed exceptional long-term stability at 5.0 and 10.0C with capacity fading rates of 0.043 and 0.029% per cycle even after 900 cycles, respectively. Effectively, even with high sulfur loading of 4.2 mg cm^{-2} and a low E/S ratio, the N,P-rGO/h-MoO$_2$@S obtained a high initial partial discharge capacity of 5.0 mAh cm^{-2} and stable cycle performance with a relatively low fading rate of 0.08% per cycle. These findings demonstrated the potential of POM as a multifunctional precursor in the formation of a redox mediator of LSB, as well as the utility of LSB as an advanced energy storage system.

Author statement

Won Il Kim contributed to Validation, Investigation, Data Curation, and Writing - Original Draft. Jeong Seok Yeon contributed to Conceptualization, Validation, Investigation, and Writing - Original Draft. Hwi Jung Kim contributed to Methodology, Software, Validation, Investigation, and Writing - Review & Editing. Hyunyoung Park contributed to Formal analysis and Writing - Review & Editing. Jongsoon Kim contributed to Supervision and Resources. Ho Seok Park contributed to Conceptualization, Writing - Review & Editing, Supervision, Resources, Project administration, and Funding acquisition.

Declaration of competing interest

The authors declare that they have no known competing financial interests or personal relationships that could have appeared to influence the work reported in this paper.

Data availability

Data will be made available on request.

Appendix A. Supplementary data

Supplementary data to this article can be found online at https://doi.org/10.1016/j.compositesb.2023.110886.

References

[1] Manthiram A, Fu Y, Chung SH, Zu C, Su YS. Rechargeable lithium-sulfur batteries. Chem Rev 2014;114(23):11751–87.

[2] Peng L, Wei Z, Wan C, Li J, Chen Z, Zhu D, et al. A fundamental look at electrocatalytic sulfur reduction reaction. Nat. Catal. 2020;3(9):762–70.

[3] Jana M, Xu R, Cheng X-B, Yeon JS, Park JM, Huang J-Q, et al. Rational design of two-dimensional nanomaterials for lithium–sulfur batteries. Energy Environ Sci 2020;13(4):1049–75.

[4] Yeon JS, Yun S, Park JM, Park HS. Surface-Modified sulfur nanorods immobilized on radially assembled open-porous graphene microspheres for lithium-sulfur batteries. ACS Nano 2019;13(5):5163–71.

[5] Liu Q, Han X, Zheng Z, Xiong P, Jeong RG, Kim G, et al. Crystallinity regulated functional separator based on bimetallic NixFey alloy nanoparticles for facilitated redox kinetics of lithium–sulfur batteries. Adv Funct Mater 2022;32(47):2207094.

[6] Xie J, Li BQ, Peng HJ, Song YW, Zhao M, Chen X, et al. Implanting atomic cobalt within mesoporous carbon toward highly stable lithium-sulfur batteries. Adv Mater 2019;31(43):e1903813.

[7] Tian Y, Li G, Zhang Y, Luo D, Wang X, Zhao Y, et al. Low-bandgap Se-deficient antimony selenide as a multifunctional polysulfide barrier toward high-performance lithium-sulfur batteries. Adv Mater 2020;32(4):e1904876.

[8] Yeon JS, Ko YH, Park TH, Park H, Kim J, Park HS. Multidimensional hybrid architecture encapsulating cobalt oxide nanoparticles into carbon nanotube branched nitrogen–doped reduced graphene oxide networks for lithium–sulfur batteries. Energy Environ Mater 2021;5(2):555–64.

[9] Zheng M, Chi Y, Hu Q, Tang H, Jiang X, Zhang L, et al. Carbon nanotube-based materials for lithium–sulfur batteries. J Mater Chem 2019;7(29):17204–41.

[10] Kim Y, Kim WI, Park H, Kim JS, Cho H, Yeon JS, et al. Multifunctional polymeric phthalocyanine-coated carbon nanotubes for efficient redox mediators of lithium–sulfur batteries. Adv Energy Mater 2023;13(22):2204353.

[11] Tian W, Xi B, Feng Z, Li H, Feng J, Xiong S. Sulfiphilic few-layered MoSe$_2$ nanoflakes decorated rGO as a highly efficient sulfur host for lithium-sulfur batteries. Adv Energy Mater 2019;9(36):1901896.

[12] Cheng Z, Xiao Z, Pan H, Wang S, Wang R. Elastic sandwich-type rGO-VS$_2$/S composites with high tap density: structural and chemical cooperativity enabling lithium-sulfur batteries with high energy density. Adv Energy Mater 2018;8(10):1702337.

[13] Li Z, Guan BY, Zhang J, Lou XW. A compact nanoconfined sulfur cathode for high-performance lithium-sulfur batteries. Joule 2017;1(3):576–87.

[14] Shi H, Ren X, Lu J, Dong C, Liu J, Yang Q, et al. Dual-function hollow carbon nanoreactors with encaged atomic zinc decorated for kinetically accelerated polysulfides conversion and dendrite free lithium sulfur batteries. Adv Energy Mater 2020;10(39):2002271.

[15] Boyjoo Y, Shi H, Olsson E, Cai Q, Wu ZS, Liu J, et al. Molecular-level design of pyrrhotite electrocatalyst decorated hierarchical porous carbon spheres as nanoreactors for lithium–sulfur batteries. Adv Energy Mater 2020;10(20):2000651.

[16] Li BQ, Zhang SY, Kong L, Peng HJ, Zhang Q. Porphyrin organic framework hollow spheres and their applications in lithium-sulfur batteries. Adv Mater 2018;30(23):e1707483.

[17] Yao S, He Y, Wang Y, Bi M, Liang Y, Majeed A, et al. Porous N-doped carbon nanofibers assembled with nickel ferrite nanoparticles as efficient chemical anchors and polysulfide conversion catalyst for lithium-sulfur batteries. J Colloid Interface Sci 2021;601:209–19.

[18] Yao S, Zhang C, Xie F, Xue S, Gao K, Guo R, et al. Hybrid membrane with SnS$_2$ nanoplates decorated nitrogen-doped carbon nanofibers as binder-free electrodes with ultrahigh sulfur loading for lithium sulfur batteries. ACS Sustainable Chem Eng 2020;8(7):2707–15.

[19] Fang R, Chen K, Yin L, Sun Z, Li F, Cheng H-M. The regulating role of carbon nanotubes and graphene in lithium-ion and lithium-sulfur batteries. Adv Mater 2019;31(9):1800863.

[20] Rana HH, Jana M, Yeon JS, Park JH, Qing L, Park HS. Interfacially polymerized polyamide interlayer onto ozonated carbon nanotube networks for improved stability of sulfur cathodes. ChemSusChem 2020;13(9):2471–8.

[21] Wang J, Han WQ. A Review of heteroatom doped materials for advanced lithium–sulfur batteries. Adv Funct Mater 2021;32(2):2107166.

[22] Yao S, Guo R, Xie F, Wu Z, Gao K, Zhang C, et al. Electrospun three-dimensional cobalt decorated nitrogen doped carbon nanofibers network as freestanding electrode for lithium/sulfur batteries. Electrochim Acta 2020;337:135765.

[23] Yao S, Xue S, Peng S, Jing M, Shen X, Li T, et al. Electrospun zeolitic imidazolate framework-derived nitrogen-doped carbon nanofibers with high performance for lithium-sulfur batteries. Int J Energy Res 2019;43(5):1892–902.

[24] Liu R, Liu W, Bu Y, Yang W, Wang C, Priest C, et al. Conductive porous laminated vanadium nitride as carbon-free hosts for high-loading sulfur cathodes in lithium-sulfur batteries. ACS Nano 2020;14(12):17308–20.

[25] Xu G, Li Y, Cheng H, Liu G, Yang Z, Gao G. Core–shell structured $S@CuO/\delta-MnO_2$ composites as cathodes for lithium–sulfur batteries. CrystEngComm 2021;23(46):8071–6.

[26] Liu Q, Jiang Q, Jiang L, Peng J, Gao Y, Duan Z, et al. Preparation of $SnO_2@rGO/CNTs/S$ composite and application for lithium-sulfur battery cathode material. Appl Surf Sci 2018;462:393–8.

[27] Yeon JS, Park TH, Ko YH, Sivakumar P, Kim JS, Kim Y, et al. 2D spinel $ZnCo_2O_4$ microsheet-coated functional separator for promoted redox kinetics and inhibited polysulfide dissolution. J Energy Chem 2021;55:468–75.

[28] Zhang C, He Y, Wang Y, Liang Y, Majeed A, Yang Z, et al. $CoFe_2O_4$ nanoparticles loaded N-doped carbon nanofibers networks as electrocatalyst for enhancing redox kinetics in Li-S batteries. Appl Surf Sci 2021;560:149908.

[29] Yao S, Bi M, Yu H, Zhang C, Zhang X, Liu H, et al. Spinel manganese-cobalt oxide nanospheres anchored on nitrogen-containing carbon nanofibers as a highly efficient redox electrocatalyst in lithium/polysulfides batteries. Appl Surf Sci 2022;598:153787.

[30] He J, Luo L, Chen Y, Manthiram A. Yolk-shelled $C@Fe_3O_4$ nanoboxes as efficient sulfur hosts for high-performance lithium-sulfur batteries. Adv Mater 2017;29(34):1702707.

[31] Liu F, Xiao Q, Wu HB, Sun F, Liu X, Li F, et al. Regenerative polysulfide-scavenging layers enabling lithium-sulfur batteries with high energy density and prolonged cycling life. ACS Nano 2017;11(3):2697–705.

[32] Hu L, Dai C, Liu H, Li Y, Shen B, Chen Y, et al. Double-shelled NiO-$NiCo_2O_4$Heterostructure@Carbon hollow nanocages as an efficient sulfur host for advanced lithium-sulfur batteries. Adv Energy Mater 2018;8(23):1800709.

[33] Ji X, Evers S, Black R, Nazar LF. Stabilizing lithium-sulphur cathodes using polysulphide reservoirs. Nat Commun 2011;2:325.

[34] Wang H, Hamanaka S, Nishimoto Y, Irle S, Yokoyama T, Yoshikawa H, et al. In operando X-ray absorption fine structure studies of polyoxometalate molecular cluster batteries: polyoxometalates as electron sponges. J Am Chem Soc 2012;134(10):4918–24.

[35] Horn MR, Singh A, Alomari S, Goberna-Ferrón S, Benages-Vilau R, Chodankar N, et al. Polyoxometalates (POMs): from electroactive clusters to energy materials. Energy Environ Sci 2021;14(4):1652–700.

[36] Kresse G. Efficiency of ab-initio total energy calculations for metals and semiconductors using a plane-wave basis set. Comput Mater Sci 1996;6:15–50.

[37] Blochl PE. Projector augmented-wave method. Phys Rev B Condens Matter 1994;50(24):17953–79.

[38] Perdew JP. Generalized gradient approximation made simple. Amer Phys Soc 1996;77(18):3865.

[39] Grimme S, Antony J, Ehrlich S, Krieg H. A consistent and accurate ab initio parametrization of density functional dispersion correction (DFT-D) for the 94 elements H-Pu. J Chem Phys 2010;132(15):154104.

[40] Niu S, Zhou G, Lv W, Shi H, Luo C, He Y, et al. Sulfur confined in nitrogen-doped microporous carbon used in a carbonate-based electrolyte for long-life, safe lithium-sulfur batteries. Carbon 2016;109:1–6.

[41] Bridgeman AJ. Computational study of the vibrational spectra of alpha- and beta-Keggin polyoxometalates. Chemistry 2004;10(12):2935–41.

[42] Bhaskar A, Deepa M, Rao TN, Varadaraju UV. Enhanced nanoscale conduction capability of a MoO_2/Graphene composite for high performance anodes in lithium ion batteries. J Power Sources 2012;216:169–78.

[43] Zhang Y, Chen X, Cen W, Ren W, Guo H, Wu S, et al. Flash-assisted doping graphene for ultrafast potassium transport. Nano Res 2022;15(5):4083–90.

[44] Zou L, Qiao Y, Wu X-S, Ma C-X, Li X, Li CM. Synergistic effect of titanium dioxide nanocrystal/reduced graphene oxide hybrid on enhancement of microbial electrocatalysis. J Power Sources 2015;276:208–14.

[45] Qu H, Zhang J, Du A, Chen B, Chai J, Xue N, et al. Multifunctional sandwich-structured electrolyte for high-performance lithium-sulfur batteries. Adv Sci 2018;5(3):1700503.

[46] Liu Q, Han X, Park H, Kim J, Xiong P, Yuan H, et al. Layered double hydroxide quantum dots for use in a bifunctional separator of lithium-sulfur batteries. ACS Appl Mater Interfaces 2021;13(15):17978–87.

[47] Hua W, Shang T, Li H, Sun Y, Guo Y, Xia J, et al. Optimizing the p charge of S in p-block metal sulfides for sulfur reduction electrocatalysis. Nat. Catal. 2023;6(2):174–84.

[48] Ma F, Srinivas K, Zhang X, Zhang Z, Wu Y, Liu D, et al. Mo_2N quantum dots decorated N-doped graphene nanosheets as dual-functional interlayer for dendrite-free and shuttle-free lithium-sulfur batteries. Adv Funct Mater 2022;32(40):2206113.

[49] Zhao Z, Yi Z, Li H, Pathak R, Cheng X, Zhou J, et al. Understanding the modulation effect and surface chemistry in a heteroatom incorporated graphene-like matrix toward high-rate lithium–sulfur batteries. Nanoscale 2021;13(35):14777–84.

[50] Ji L, Wang J, Teng X, Dong H, He X, Chen ZN. P-doped molybdenum carbide nanofibers for efficient hydrogen production. ACS Appl Mater Interfaces 2018;10(17):14632–40.

[51] Feng Y, Liu H, Zhao F, Liu Y, Li J, Liu X. Simultaneous defect-engineered and thiol modified of MoO_2 for improved catalytic activity in lithium-sulfur batteries: a study of synergistic polysulfide adsorption-conversion function. Chem Eng J 2021;409:128177.

[52] Luo D, Li C, Zhang Y, Ma Q, Ma C, Nie Y, et al. Design of quasi-MOF nanospheres as a dynamic electrocatalyst toward accelerated sulfur reduction reaction for high-performance lithium-sulfur batteries. Adv Mater 2022;34(2):e2105541.

[53] Moy D, Manivannan A, Narayanan SR. Direct measurement of polysulfide shuttle current: a window into understanding the performance of lithium-sulfur cells. J Electrochem Soc 2014;162(1):A1–7.

[54] Zhou X, Meng R, Zhong N, Yin S, Ma G, Liang X. Size-dependent cobalt catalyst for lithium sulfur batteries: from single atoms to nanoclusters and nanoparticles. Small Methods 2021;5(10):e2100571.

[55] Cruz-Silva E. Heterodoped nanotubes theory synthesis, and characterization of phosphorus. ACS Nano 2008;2(3):441–8.